Engineering Structures 351 (2026) 121956

Contents lists available at ScienceDirect

Engineering Structures

journal homepage: www.elsevier.com/locate/engstruct

Thermo-electro-mechanical bending of submarine power cables

Pan Fang [a,b,c,*], Xiao Li [d], Xiaoli Jiang [a], Hans Hopman [a], Yong Bai [c]

[a] *Department of Maritime and Transport Technology, Delft University of Technology, Netherlands*
[b] *Department of Materials, Textiles and Chemical Engineering (MaTCh), Ghent University, Technologiepark-Zwijnaarde 46/70, Zwijnaarde, B-9052, Belgium*
[c] *College of Civil Engineering and Architecture, Zhejiang University, Hangzhou, Zhejiang, PR China*
[d] *Institute of High Performance Computing (IHPC), Agency for Science, Technology and Research (A*STAR), 1 Fusionopolis Way, #16-16 Connexis, Singapore 138632, Republic of Singapore*

ARTICLE INFO

Keywords:
Finite element modeling
Multi-physical simulation
Contact mechanics
Repetitive unit cell (RUC)
Temperature-dependent cross-linked polyethylene (XLPE)
Submarine power cable bending

ABSTRACT

Submarine power cables (SPCs) experience complex multi-physical effects in practical engineering scenarios, particularly involving mechanical, thermal, and electrical interactions. When electrical current passes through inner conductors, temperature rises induce thermal expansion, leading to deformation and influencing the bending behavior through alterations in the stick–slip mechanism. Although experimental studies have highlighted temperature's significant impact on the bending performance of SPCs, detailed insights into the underlying multi-physical interactions remain scarce. This paper introduces a novel repetitive unit cell (RUC) numerical model to investigate the bending behavior of SPCs comprehensively under coupled electrical, thermal, and mechanical fields. An innovative thermal expansion method is proposed to effectively simulate initial residual stresses present at component interfaces post-manufacturing. Furthermore, a temperature-dependent constitutive model based on the Ramberg–Osgood framework is developed and validated against experimental data obtained at varying temperatures. The simulation distinctly identifies the competing effects of material softening and contact stress variations induced by temperature changes, providing critical insights into their contributions to overall cable bending behavior. The outcomes offer valuable guidelines for engineers in the practical design and optimization of submarine power cables. All relevant computational codes developed in this study are publicly accessible at https://pan-fang.github.io/Codes/.

1. Introduction

As wind farms move into deeper and more remote ocean areas to harness abundant wind energy, submarine power cables (SPCs) must be used to carry high-voltage current under complex loading conditions. The high-voltage current within conductors generates heat, creating a temperature gradient between the SPC and the surrounding sea environment, ultimately inducing stresses within the cable [1]. When combined with mechanical loads from the environment, predicting the mechanical behavior of SPCs becomes extremely challenging. This hampers our understanding of the structure and affects cable design, especially when key physical interactions that degrade performance are overlooked [2]. For instance, heat generated by the electrical current causes thermal expansion of the cable's constituent layers, altering the interfacial contact pressures and friction. This in turn affects the cable's bending stiffness and can lead to accelerated fatigue damage, issues that are central to this investigation.

The analysis of such a complex structure under multiphysical coupling is a significant challenge, despite being recognized in various industry reports and standards [3,4]. The main physical fields involved in an operating SPC include electrical, thermal, and mechanical effects, and often magnetic effects as well. Therefore, the design and analysis of SPCs require interdisciplinary collaboration among electrical, thermal, and mechanical engineers [5]. However, most current research remains confined within individual disciplines.

From the perspective of electrical engineers, the electric and magnetic fields receive primary attention due to their strong coupling. Magnetic fields are important because they affect cable performance, can cause electromagnetic interference, and may impact marine life [6–8]. These issues are critical for both technical reliability and environmental compliance. As most components in multi-core cables are twisted helically for mechanical and electrical performance, analyzing magnetic behavior becomes even more complex. To address this, both analytical [9,10] and numerical [11,12] methods have been proposed for predicting magnetic field strength in helically-configured power cables.

Electrical engineers also need to evaluate the heat generated in the cable before thermal engineers can study heat transfer within it, resulting in coupling between electrical and thermal fields. The allowable

---

[*] Corresponding author at: Department of Maritime and Transport Technology, Delft University of Technology, Netherlands.
E-mail address: panfang@zju.edu.cn (P. Fang).

https://doi.org/10.1016/j.engstruct.2025.121956
Received 11 September 2025; Received in revised form 14 November 2025; Accepted 8 December 2025

temperature for cable operation is typically defined in standards and product specifications to ensure safety [13]. For instance, according to widely adopted standards such as IEC 60287 [14], the maximum continuous operating temperature for cross-linked polyethylene (XLPE) insulation, a common material in SPCs, is typically limited to 90 °C (363.15 K). Researchers have investigated how factors such as laying methods, seawater flow, seawater temperature, burial depth, and soil thermal conductivity influence a cable's thermal performance [15,16]. Among all components, the insulation layer receives particular attention due to its sensitivity to temperature [17]. Additionally, the thermal distribution around cable terminations differs from that of submerged cable sections, and this has been explored in the literature [18–21].

Another notable multiphysical phenomenon in electrical engineering is dielectric breakdown in insulation [22], a critical failure mode where the insulating material (usually polymer or paper-oil) loses its ability to resist current. Once breakdown occurs, current flows through the material [23]. During this process, microcracks grow and branch like a tree, referred to as electrical treeing [24]. In marine environments, moisture accelerates this process, resulting in water treeing [25]. Both phenomena are closely related to mechanical stress within the insulation, making this a multiphysical issue [26]. Several researchers have developed models to predict and analyze electrical tree growth [27–29], with phase field methods showing good predictive capabilities [30,31].

From a mechanical engineering perspective, focus is often placed on cable sections subjected to large mechanical loads, such as dynamic cables suspended from floating platforms in harsh environments. These cables may fail if mechanical loads exceed design limits. Due to SPC complexity, many mechanical studies neglect multiphysical effects [32,33]. Key challenges in SPC mechanical analysis include multiple helical components and intensive contact interactions, especially during bending where stick–slip behavior is more pronounced. Given the strong structural nonlinearity, numerical methods are favored over analytical ones [34], with 3D finite element models being widely used.

In tension studies, helical wires can often be modeled using beam elements, making full-scale modeling feasible [35]. However, under bending, helical wires involve complex contact behavior and cannot be simplified as beams. Full-scale bending models require significant computational resources. To address this, researchers [36,37] developed RUC models leveraging the periodic structure of helical components. By applying periodic boundary conditions, a short RUC segment can be modeled, significantly reducing computation time.

Bending studies [33,36] have identified initial residual stress as a key factor affecting SPC mechanical response. Residual stress arises during manufacturing due to temperature gradients in the polymer material and affects stick–slip behavior at interfaces. Unlike residual stresses in metals [38–40], residual stress in polymers has received little research attention. In practice, residual stress is often calibrated using bending moment–curvature test data. These curves show two segments: a stick phase and a slip phase [34,41]. During the stick phase, frictional forces prevent slippage; as curvature increases, friction becomes insufficient, initiating slip. According to Coulomb's law, friction force is linked to normal force, meaning temperature-induced deformation in polymers can significantly influence SPC bending behavior.

Experimental investigations by Maioli et al. [42], Tyrberg et al. [43], and Komperød and Magnus [44] have examined the influence of temperature on the mechanical behavior of SPCs. For example, Komperød and Magnus reported that increasing the ambient temperature from 5°C to 20°C resulted in a reduction of bending moment by approximately 50%. Such temperature-induced softening can significantly affect cable performance, and if not properly accounted for, may lead to overbending failures [45]. However, while these tests demonstrate a clear correlation between temperature and bending response, they do not reveal the internal mechanisms responsible for the observed changes in stiffness or deformation behavior.

In contrast to experimental methods, numerical modeling offers a more effective approach for uncovering internal mechanisms and multiphysical interactions. Despite this advantage, detailed numerical analyses of full-scale, multilayer SPCs under coupled thermal–mechanical loading remain scarce. Existing studies on other systems can be found in the open literature, such as the thermoelastic behavior analysis of bonded cables [46–48] or basic thermal–mechanical responses of composite materials [49,50]. Drissi-Habti et al. [51] employed numerical simulations to study the bending effects on composite cables interacting with irregular seabed topography, highlighting the utility of computational models in predicting mechanical behavior. Some efforts have modeled SPCs using two-dimensional finite element frameworks under electro-thermal–mechanical coupling [52–54], yet these studies did not incorporate contact stresses arising from thermal expansion, and thus failed to capture the stick–slip issue in multi-layer structures that influences on bending behavior. Fouad Ech-Cheikh et al. [55] also investigated helical cable behavior under thermal loading, but similarly neglected interfacial contact stresses. As a result, the multiphysical coupling effects and internal deformation mechanisms of SPCs remain poorly understood. In practical applications, SPCs often behave as "black boxes", with design decisions heavily reliant on empirical rules that may lead to unexpected or premature failures.

In this paper, the bending behavior of an SPC under multiphysical fields is comprehensively studied using numerical methods. The structure of the paper is as follows: Section 2 presents bending tests used to calibrate initial residual stress and material tests under varying temperatures. Section 3 introduces a temperature-dependent constitutive model for insulation. Section 4 outlines the finite element model used for the simulations. Section 5 details the calibration of residual stress using experimental data. Section 6 presents the bending analysis under electro-thermal-mechanical coupling. Parametric studies are performed in Section 7. Finally, Section 8 summarizes the findings and concludes the study.

2. Tests

The test submarine power cable corresponds to the standard labeling [14,56] as "CU/SC-XLPE/XLPE/SC-XLPE/CU/MDPE 35 kV 1C", where CU denotes the copper conductor, SC-XLPE represents semi-conducting cross-linked polyethylene shields, XLPE is the insulation layer, and MDPE is the outer sheath. Detailed parameters, including layer thicknesses and material specifications, are provided in Table 1. A schematic of the cable's cross-section is shown in Fig. 1. The cable is rated for a nominal voltage of 35 kV and features a single-core configuration with an 11.4 mm diameter copper conductor. It should be noted that the actual conductor is of a stranded construction, which is simplified in the numerical model as a solid cylinder with an equivalent outer diameter of 11.4 mm. The insulation system comprises semi-conducting XLPE shields and a main XLPE insulation layer, while mechanical protection is provided by a copper wire screen and MDPE-based waterproofing and outer sheath layers. Bending and material characterization tests were conducted and are detailed in Section 2.1 and Section 2.2, respectively. The former presents bending moment–curvature data used to calibrate initial residual stress in the cable, while the latter provides temperature-dependent material properties as input for the numerical model.

2.1. Bending test

Bending tests were conducted on single-core SPC samples to obtain the bending moment–curvature relationship. A four-point bending setup was employed on four cable specimens, each loaded until reaching a final curvature of 1×10^{-3}/mm. As illustrated in Fig. 2(a), two fixed supports held the cable specimen vertically, while two loading heads applied vertical forces. Three displacement sensors were positioned beneath the cable to measure vertical displacements at three key

Table 1
Nominal design parameters of the cable specimens.

Layer	Component	Thickness (mm)	Outer diameter (mm)	Materials
1	Copper conductor	–	11.4	Copper
2	Conductor shield	0.8	13.0	Semi-conducting XLPE
3	Insulation	10.5	34.0	XLPE
4	Insulation shield	1.0	36.0	Semi-conducting XLPE
5	Water-proof layer	0.45	36.9	MDPE
6	Copper wire	1.15	39.2	Copper
7	Copper shield	0.2	39.6	Copper
8	Water-proof layer	0.45	40.5	MDPE
9	Sheath	2.5	45.5	MDPE

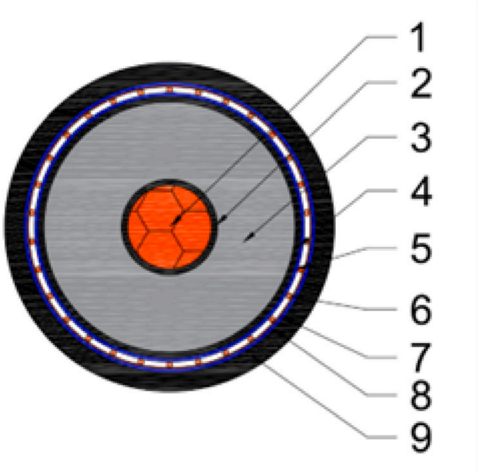

Fig. 1. Cross section of the submarine power cable.

points. These points define a circle, from which curvature was calculated. Each test specimen measured 600 mm in length. The detailed geometric configuration is shown in Fig. 2(b). The resulting bending moment–curvature curves for the four specimens are presented in Fig. 2(c).

Dynamic power cables are typically designed with a minimum bend radius, beyond which mechanical failure may occur; operational curvature must remain below this threshold [57]. According to Chen et al. [58], the minimum allowable bending radius is 20 times the outer diameter of the cable, equivalent to 910 mm in this case. This corresponds to a maximum curvature of approximately 1×10^{-3}/mm, which matches the limit applied in the test. This conservative limit is stricter than that recommended in relevant standards [3], as multiphysical effects may reduce cable performance and increase the risk of failure. Therefore, the bending radius was deliberately kept within a safer range to ensure the cable operated under healthy conditions.

2.2. Material test

To complement previous tests on polymers at room temperature [59], material tests in this study focused on investigating the temperature-dependent behavior of the XLPE insulation layer. This focus was motivated by several factors: (1) the insulation layer is in direct contact with the primary heat source—the copper conductor; (2) it constitutes a significant portion of the cable's cross-sectional volume, making its properties highly influential on the overall thermo-mechanical response; and (3) its polymeric nature makes it more sensitive to temperature variations compared to metals. The mechanical properties of the copper conductor and the MDPE sheath were considered temperature-independent and were sourced from manufacturer data and our previous work [59], respectively.

Since polymer properties may change after extrusion into a cylindrical form, the test specimens were cut directly from the cable samples. They were machined into dumbbell-shaped specimens according to the dimensions specified in ISO 527-2012 [60], as illustrated in Fig. 3(a). An image of the dumbbell-shaped insulation samples is shown in Fig. 3(b). Six groups of specimens were prepared, labeled Group A through Group F, with each group containing five specimens. Group F was reserved to supplement any earlier group in case of test failure.

The test temperatures ranged from 293.15 K to 373.15 K, with increments of 20 K. This range was specifically chosen to cover the full spectrum of the cable's operational conditions, from typical ambient seawater/air temperatures to the maximum continuous operating temperature of 90 °C for XLPE insulation, as stipulated by industry standards [14], and also to account for potential short-term overload scenarios. A sealed chamber with temperature control capabilities was used for the tests, as shown in Fig. 3(c). An electronic universal testing machine was installed inside the chamber to measure specimen elongation and the force applied at the specimen ends. The specimens were placed in the chamber prior to testing to ensure they reached the target temperature before loading commenced.

From these tests, stress–strain curves were obtained. The testing machine had a maximum capacity of 2.5 kN, and the loading speed was maintained at a constant rate of 5 mm/min for all specimens, representing quasi-static loading conditions. It is acknowledged that the mechanical response of polymeric materials like XLPE can exhibit rate-dependency (viscoelasticity), particularly at elevated temperatures. The constitutive model developed in this study is therefore calibrated for and applicable to quasi-static or low-frequency loading scenarios. A full investigation of the strain-rate effects was beyond the scope of this work. After testing, the stress–strain data for each sample were processed using linear interpolation and averaging methods. The true stress and true strain were then calculated according to the following equations:

$$\epsilon_{True} = \ln(1 + \epsilon_{Nominal}) \tag{1}$$

$$\sigma_{True} = \sigma_{Nominal}(1 + \epsilon_{Nominal}) \tag{2}$$

The material properties of XLPE will be further processed in the following section for the model input in our cable simulation.

3. Material constitutive model for insulation

This section describes the material constitutive models used for the main components of the SPC. The key mechanical properties for copper, MDPE, and the temperature-dependent model for XLPE are presented. For the copper conductor and the MDPE outer sheath, temperature-independent elastic–plastic models were used. According to specifications provided by the cable manufacturer, the copper conductor has a Young's modulus of 90 GPa, a Poisson's ratio of 0.32, and a yield strength of 130 MPa. The material properties of MDPE, based on our previous experimental work [59], are defined by a Young's modulus of 200 MPa and a Poisson's ratio of 0.45, with its non-linear stress–strain behavior detailed in [59]. The primary focus of the material

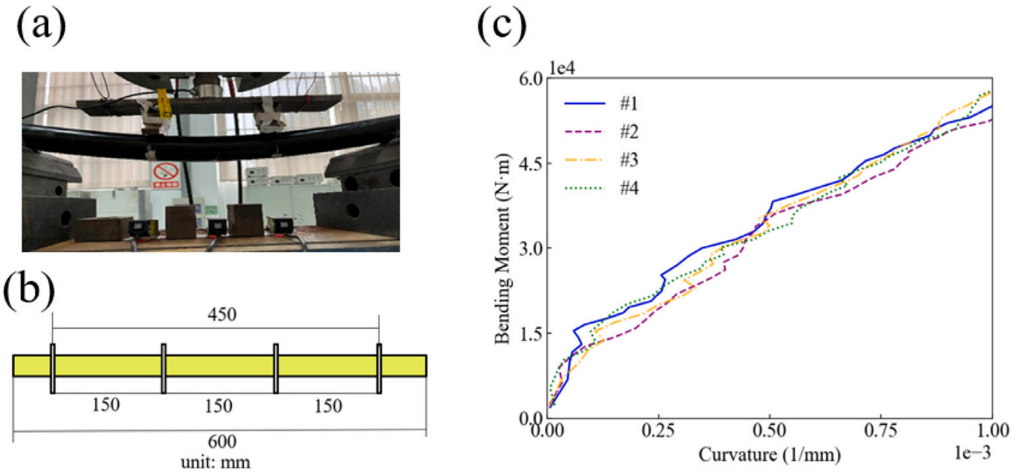

Fig. 2. Bending test regarding the SPC sample. (a) Bending test setup; (b) the dimension of the cable sample for bending test; (c) the curvature-bending moment for four samples from the bending test.

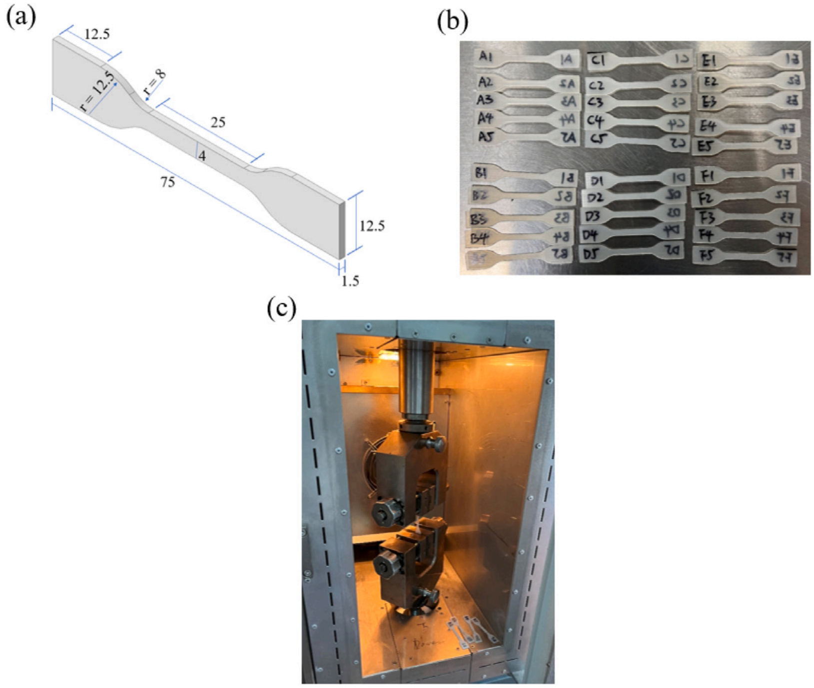

Fig. 3. The test of insulation under different temperatures. (a) The size of the insulation sample; (b) the cut samples from the cable; (c) the universal testing machine in a sealed box with temperature regulated.

characterization in this study was on the XLPE insulation, for reasons detailed in Section 2.2. A temperature-dependent constitutive model was developed for XLPE, and its formulation is described in Section 3.1. Section 3.2 presents its validation.

3.1. Development of the constitutive model

The insulation occupies a large portion of the cable cross-section and is in direct contact with the copper conductor, which generates heat during operation. Therefore, the temperature-dependent material behavior of XLPE must be considered. In this study, stress–strain curves for XLPE at various temperatures were obtained through material testing. A major challenge in finite element modeling (FEM) is the proper incorporation of temperature-dependent material properties. Following the methodology proposed by Duan et al. [61], the Ramberg–Osgood model was employed to describe the constitutive behavior:

$$\epsilon_t = \epsilon_e + \epsilon_p = \frac{\sigma}{E(T)} + \left(\frac{\sigma}{K(T)}\right)^{g(T)} \tag{3}$$

where σ is the stress, E is the Young's modulus, K is the nonlinear modulus, and g is the hardening exponent. All three parameters (E, K, and g) are temperature-dependent and were fitted based on the experimental data collected at different temperatures. For each material test curve from the five groups, the corresponding E, K, and g values were extracted and fitted using linear regression, as illustrated in Fig. 4. The resulting fitted equations are:

$$\begin{aligned} E &= -1.35T + 513.91 \\ K &= -0.13T + 50.75 \\ g &= -0.05T + 19.95 \end{aligned} \tag{4}$$

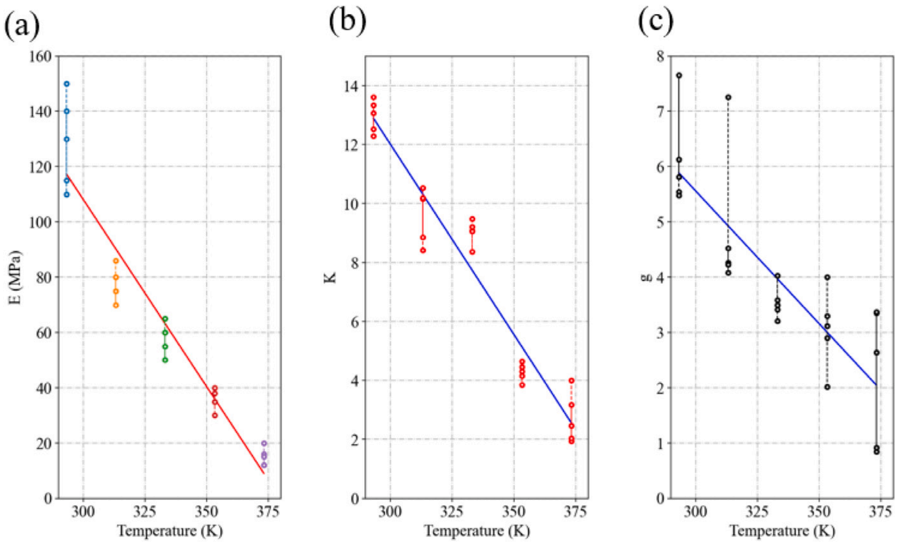

Fig. 4. Temperature-dependent parameters in the Ramberg–Osgood model: (a) E; (b) K; and (c) g.

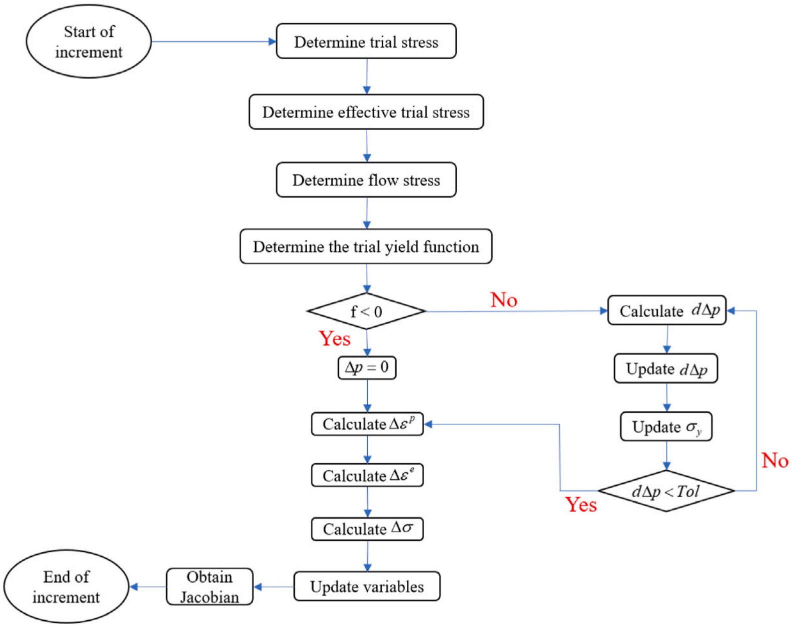

Fig. 5. Flowchart for implementing the temperature-dependent material model.

To implement the temperature-dependent behavior, a user-defined material subroutine (UMAT) was developed for ABAQUS/Standard [62]. The development process is summarized in the flowchart shown in Fig. 5. The UMAT code is freely available for download.

3.2. Validation of the constitutive model

To validate the developed constitutive model, a dumbbell-shaped specimen model was created, matching the dimensions used in the material tests (Fig. 3(a)). Simulations were performed to generate stress–strain curves at different temperatures, and the results were compared with the experimental data, as shown in Fig. 6. For each group, the experimental results were averaged to facilitate comparison.

The strain was calculated based on the relative displacement between two points in the effective gauge section of the dumbbell specimen (25 mm in length, as shown in Fig. 3(a)), ensuring consistency between experimental and simulation procedures. True stress and true strain values were calculated for both the experimental and simulated results.

The results demonstrate that the material exhibits strong temperature dependence: as the temperature increases, the material becomes more flexible. The developed constitutive model showed good agreement with the experimental results, validating its accuracy. This model will be employed in the subsequent finite element analysis of the insulation layer in the submarine power cable, where temperature effects are significant.

4. Finite element model for SPC

The detailed cross-section of the SPC, as shown in Fig. 1, includes several thin functional layers, such as the conductor shield, insulation shield, and water-proof layers. To enhance computational efficiency while capturing the primary bending mechanics, these thin layers were integrated into adjacent, thicker primary layers in the finite element model. For example, the semi-conducting XLPE shields were merged

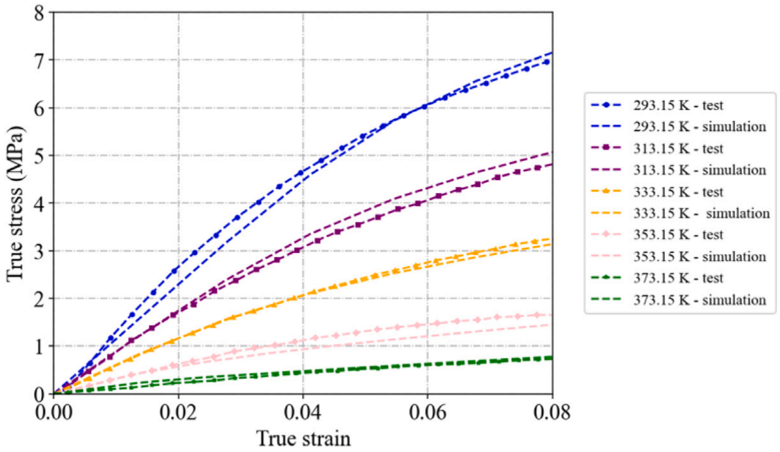

Fig. 6. Stress–strain curves of the dumbbell specimen at different temperatures: experimental vs. simulation results.

Table 2
Parameters and materials used in the simplified model.

Layer	Thickness (mm)	Outer diameter (mm)	Material
I	–	11.4	Copper
II	12.75	36.9	XLPE
III	1.15	39.2	Copper
IV	3.15	45.5	MDPE

Table 3
Parameters related to electrical and thermal fields.

Property	Copper	XLPE	MDPE
Thermal conductivity	398 W/(m K)	0.286 W/(m K)	0.286 W/(m K)
Expansion coefficient	1.64×10^{-5}/K	2×10^{-4}/K	2×10^{-4}/K
Electrical conductivity	5.8×10^{7} S/m	1×10^{-11} S/m	1×10^{-11} S/m

with the main XLPE insulation, as they share similar material properties and are typically co-extruded and bonded, thus preventing significant interfacial slip. The dimensions of the simplified cross-section are listed in Table 2.

This modeling simplification is based on the assumption that the global bending stiffness and the stick–slip behavior are predominantly governed by the interfaces between the major structural components (i.e., conductor, insulation, helical wires, and outer sheath). However, we acknowledge the implications of this approach. By neglecting these discrete layers, our model does not capture the localized stress concentrations or potential micro-slip phenomena that might occur at these specific interfaces. This could lead to a slight overestimation of the composite stiffness of the insulation system and simplifies the frictional landscape within the cable assembly. Nevertheless, this approach is considered appropriate for investigating the macroscopic thermo-mechanical bending response, which is the focus of this study. Engineers interested in the detailed effects of these minor layers can build upon the current modeling framework to incorporate them.

To capture the electrical and thermal fields, additional properties including thermal conductivity, electrical conductivity, and thermal expansion coefficient were incorporated. These parameters, referenced from [63–66], are summarized in Table 3. One main goal of this study is to demonstrate the modeling of multiphysical effects through an RUC model and to reveal the influence of these effects on the bending behavior of SPCs. Engineers can achieve more accurate predictions by refining these parameters through laboratory testing.

The finite element model was developed using periodic boundary conditions to reduce the model to a short RUC [67]. The principles and detailed development of the RUC model have been discussed in previous studies [32,59]. Interested readers can refer to [68–71] for more information on periodic boundary methods. The RUC length was determined according to:

$$l = k\frac{p_i}{m_i} \tag{5}$$

where $k \in \mathbb{N}$, p_i is the pitch length, and m_i is the number of helices in layer i. For single-core SPCs, helical structures exist only in the armor layers; thus, the model length depends solely on the armor configuration. There are 40 helical wires with corresponding pitch length of 400 mm. The RUC length was determined to be 40 mm to get rid of possible boundary effects. Modeling was performed in ABAQUS/Standard (2022) using a static analysis scheme [72].

4.1. Physical problem definition

SPCs under real-world conditions involve three coupled physical fields: electrical, thermal, and mechanical. The interactions between these fields can be complex, with some being strongly coupled while others are weak. In this study, we adopt what is often referred to as a 'weak-coupling' or 'sequential-coupling' approach. Specifically, we focus on the influence of the thermo-electrical fields on the mechanical behavior, which is the primary concern for the structural integrity of the cable. The feedback from the mechanical field — such as strain-induced changes in electrical resistivity or thermal conductivity — is neglected.

The coupling relationships modeled in this study are illustrated in Fig. 7. The primary pathway is as follows: an applied electrical potential leads to Joule heating in the conductor (electro-thermal coupling), which in turn creates a temperature field. This temperature field then induces mechanical stresses through thermal expansion and by altering temperature-dependent material properties (thermo-mechanical coupling). Our analysis, therefore, concentrates on this dominant, one-way causal chain.

Thermal and electrical boundary conditions were selected based on IEC 60287 [14], IEC TR 62095 [56] and the specification of the product set by the manufacturer, assuming steady-state conditions. The continuous operating temperature of the XLPE insulation was set to remain below 353.15 K, consistent with industry standards and cable specification.

Despite the one-way coupling illustrated, simulations were conducted using a fully coupled thermal-electrical-structural analysis scheme in ABAQUS [73], involving a nonsymmetric Jacobian matrix solved through Newton's method:

$$\begin{bmatrix} K_{uu} & K_{u\varphi} & K_{u\theta} \\ K_{\varphi u} & K_{\varphi\varphi} & K_{\varphi\theta} \\ K_{\theta u} & K_{\theta\varphi} & K_{\theta\theta} \end{bmatrix} \begin{Bmatrix} \Delta u \\ \Delta\varphi \\ \Delta\theta \end{Bmatrix} = \begin{Bmatrix} R_u \\ R_\varphi \\ R_\theta \end{Bmatrix} \tag{6}$$

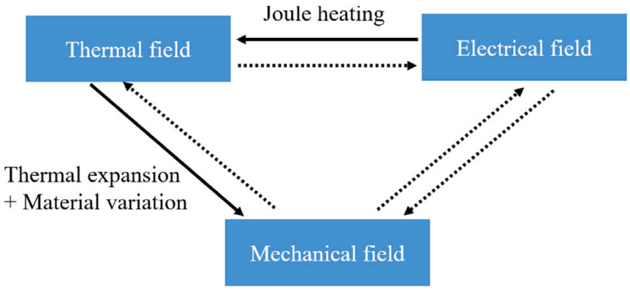

Fig. 7. Coupling relationships between heat transfer, electricity, and mechanical behavior.

Here, Δu, $\Delta\varphi$, and $\Delta\theta$ are corrections to displacement, electric potential, and temperature, respectively, and R_u, R_φ, and R_θ are the corresponding residuals.

Three analysis steps were employed for numerical stability (Fig. 8): 1. Apply a small external pressure to promote initial contact between layers. 2. Apply an electric potential difference to simulate Joule heating and induce residual stresses. 3. Apply a bending angle to analyze mechanical response.

4.2. Mesh and interaction

Since electrical, thermal, and mechanical fields must be considered simultaneously, the finite elements selected must be capable of capturing multiphysical effects. All components were meshed using Q3D8 elements (8-node bricks with trilinear displacement, electric potential, and temperature degrees of freedom) [74]. The final mesh, presented in Fig. 9, was determined through a mesh sensitivity study to ensure the convergence of the results while maintaining computational efficiency. Three different mesh densities were evaluated: a coarse mesh (8 element layers along the axial direction), a medium mesh (14 axial layers, as adopted), and a fine mesh (20 axial layers). The study compared the peak bending moment at the final curvature and the maximum von Mises stress in the helical wires. The results showed that the deviation between the medium and fine meshes was less than 2% for these key outputs, whereas the coarse mesh showed a deviation of approximately 7%. Therefore, the medium mesh with 14 axial layers, consisting of 83,016 Q3D8 elements in total, was deemed to provide a suitable balance between accuracy and computational cost.

Hard contact was assigned in the normal direction, and a classical Coulomb friction model was used for tangential contact. Specifically, a constant friction coefficient was defined at the interfaces. In the absence of specific experimental data for the cable's interfaces, a friction coefficient of 0.2 was assumed for the main analyses. This value was selected as a representative figure based on the typical range (0.1–0.3) reported in the literature for similar polymer-metal and polymer-polymer contacts in flexible structures [75–77].

To account for initial residual stresses between layers, instead of applying an equivalent external pressure as recommended by CIGRE [78], a thermal field was introduced into the model. This induced material expansion, effectively replicating the effects of initial residual stresses.

In this study, perfect contact between adjacent concentric layers was assumed to simplify the modeling process and focus on the primary mechanisms influencing bending behavior under coupled mechanical, thermal, and electrical fields. The assumption of perfect contact has been commonly used in preliminary studies of flexible pipe or cable systems [33,79]. In practical cable constructions, small intentional gaps are often introduced to accommodate mechanical stresses and thermal expansion during installation and operation. Although explicitly modeling these gaps would yield a more accurate stress distribution, it would require highly nonlinear contact algorithms and significantly increase computational costs. This aspect will be addressed in future work to further enhance model fidelity.

4.3. Load and boundary conditions

In the RUC model, two reference points (RPs) were defined at the midpoints of both end cross sections, as illustrated in Fig. 10(b). The right RP was fully constrained, while the left RP was constrained in all directions except along the axial direction, allowing the cable to extend freely without longitudinal constraint.

Periodic boundary conditions (PBCs) were applied throughout all simulation steps, establishing relationships among nodes on the left and right surfaces and the left RP. Detailed formulations of the PBCs can be found in [32,36].

- In Step-1, a very small external pressure was applied to promote initial contact and improve convergence.

- In Step-2, an electric potential V was applied at one end of the copper conductor, while the other end was grounded (0 V), creating a voltage difference and thus an electric current (Fig. 10(a)).

- In Step-3, a bending angle θ_1 was imposed at the left RP (Fig. 10(b)), transferring the load into the structure through the periodic boundary conditions.

5. Calibration of the initial residual stress

The initial residual stress within an SPC is difficult to measure directly through testing. Therefore, CIGRE [78] recommends an equivalent approach, namely applying an external pressure to the outermost layer to simulate the resulting effect. In this study, an alternative method is proposed: simulating the initial residual stress through material expansion caused by a temperature increase induced by an applied electric potential. The magnitude of the electric potential is calibrated by comparing curvature–bending moment curves from numerical simulations with experimental bending test results.

Details of the single-core SPC bending test are provided in Section 2.1. The small-curvature portion of the experimental curvature–bending moment curves, after averaging, is redrawn in Figs. 11(a) and (b). Five simulation cases were analyzed, with the applied voltage ranging from 0 to 0.5 V in increments of 0.1 V. The curvature–bending moment curves obtained from these simulations are plotted alongside the experimental data in Fig. 11(a).

When no electric potential is applied, the curvature–bending moment relationship exhibits a straight line. In contrast, when an electric potential is applied, the curve displays two distinct linear regions, corresponding to the stick and slip phases observed in experimental results. The slope before slipping occurs is referred to as the stick stiffness, while the slope after slipping is the slip stiffness.

The curvature–bending moment behavior is highly sensitive to the applied voltage: as the voltage increases, both the stick stiffness and the bending moment corresponding to the onset of slip increase. To quantitatively evaluate the agreement between simulations and experimental data, the coefficient of determination (R^2) was used [80,81], defined as:

$$R^2 = 1 - \frac{SS_{\text{res}}}{SS_{\text{tot}}} \tag{7}$$

where

$$SS_{\text{res}} = \sum_{i=1}^{n} (y_i - \hat{y}_i)^2 \tag{8}$$

$$SS_{\text{tot}} = \sum_{i=1}^{n} (y_i - \bar{y})^2 \tag{9}$$

Here, y_i represents the experimental observations, $\hat{y}_i$ denotes the corresponding simulation predictions, and $\bar{y}$ is the mean of the experimental observations. The value of R^2 ranges from $-\infty$ to 1, with 1 indicating perfect agreement.

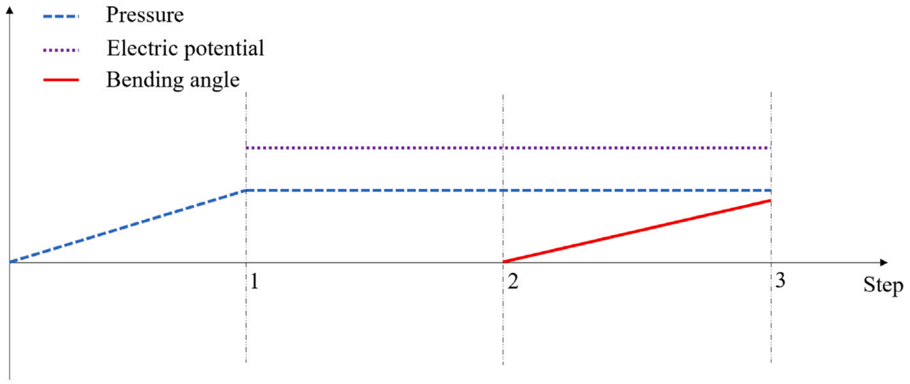

Fig. 8. Loading strategy for the thermo-electro-mechanical coupling simulation. A small pressure is applied for the convergence in Step 1 followed by an electric potential in Step 2, and finally a bending angle is applied.

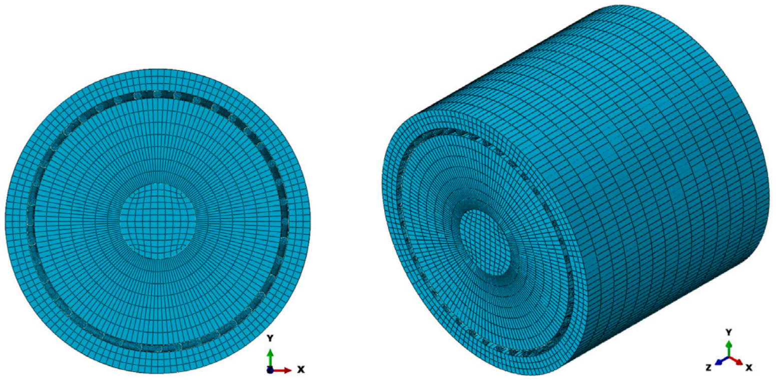

Fig. 9. Mesh results of the SPC sample.

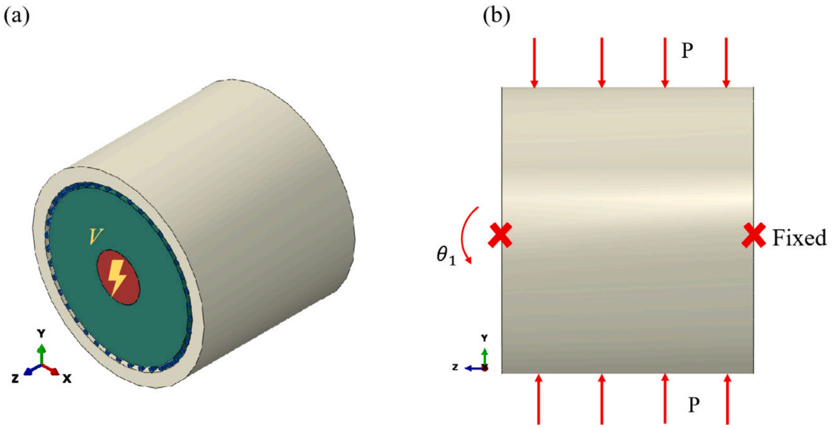

Fig. 10. Load and boundary conditions applied to the RUC model: (a) electric potential is applied in Step-2; (b) Pressure is applied from Step-1 and propagate until Step-3, while bending angle is applied in Step-3.

It was found that when the applied voltage is 0.2 V, the simulation results exhibit the best agreement with the experimental curvature–bending moment relationship. Thus, 0.2 V is calibrated as the equivalent voltage representing the initial residual stress, and this value is adopted in subsequent analyses.

To further investigate the influence of electric potential, higher voltages ranging from 1 V to 5 V (in 1 V increments) were applied. It should be noted that although the applied potentials (1–5 V) may appear small in absolute terms, they are imposed across a 40 mm cable length, resulting in high electric field intensities. This justifies the observed mechanical response, even for small potential changes. The resulting curvature–bending moment curves are shown in Fig. 11(b). As expected, the bending moment increases with increasing voltage, except when the voltage increases from 4 V to 5 V. This anomaly is attributed to local stress conditions within the helical wires, which will be discussed in detail in Section 6.

6. Mechanical studies under multiphysical effects

After calibrating the initial residual stresses, the mechanical behavior of the SPC under the influence of multiphysical fields was studied in detail. The behavior was analyzed separately during the electric potential step (Section 6.1) and the subsequent bending step (Section 6.2).

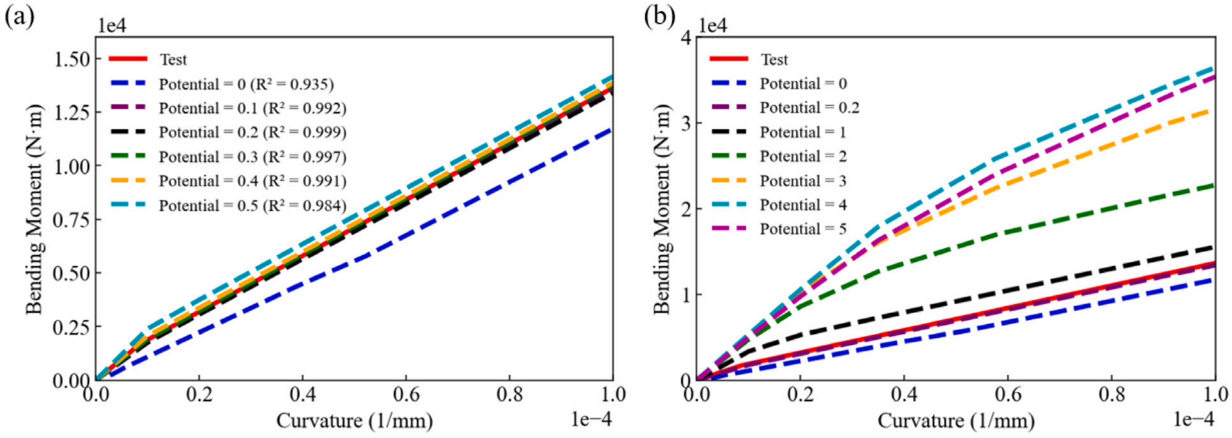

Fig. 11. Comparison of experimentally measured bending moment–curvature relationships (Test, solid red line) with simulation results under different electric potentials: (a) low voltage range (0 to 0.5 V); (b) higher voltage range (1 to 5 V). Goodness-of-fit (R^2) values comparing each simulated curve to the experimental data are indicated in the legend.

The multiphysical analysis in this study reveals a thermo-mechanical behavior that is fundamentally different from that reported in several experimental studies. Previous investigations by Maioli et al. [42] and Komperød and Magnus [44] involved heating the entire cable specimen externally (e.g., in a temperature-controlled chamber). Their results consistently showed a decrease in bending stiffness with increasing temperature, a behavior largely attributed to the thermal softening of the polymeric components.

In contrast, our study simulates the in-service condition where heat is generated internally by the conductor via Joule heating. This creates a steep temperature gradient from the core to the outer layers. As will be demonstrated, this internal heating mechanism leads to a counter-intuitive increase in bending stiffness. The following sections will detail this phenomenon and uncover the underlying physical reasons for this critical difference, highlighting the importance of accurately modeling the operational heating mode of SPCs.

6.1. Electric potential step

After applying an electric potential, the copper conductor becomes electrified, resulting in heat generation and transfer among the cable components and the ambient environment. The resulting temperature variations cause material expansion and induce changes in material properties, leading to the accumulation of stresses within the cable. The three physical fields were investigated separately.

The electrical current density across the cable cross-section is shown in Fig. 12(a). As expected, the current flows exclusively through the copper conductor because the voltage is applied only at the conductor ends, and the electrical conductivity of the polymers is extremely low. Once electrified, the conductor generates heat, which subsequently propagates through the adjacent layers. Consequently, a diffuse temperature distribution is established, as illustrated in Fig. 12(b). The conductor exhibits the highest temperature, which gradually decreases through the insulation and outer layers, approaching the ambient temperature at the outermost surface. Although the applied voltage is relatively small, resulting in a temperature increase of only 0.1 K in the conductor, this seemingly minor variation still induces a non-negligible effect on the curvature–bending moment behavior, motivating a detailed investigation of the stress distributions across the layers.

The stick–slip phenomenon observed during the bending step is strongly influenced by the contact stresses between adjacent layers. Therefore, contact stresses, particularly those acting on the insulation and outer layers, which are directly in contact with the helical wires, were extracted for analysis. To eliminate boundary effects, stress data were collected from the midsection of the model. The stress distributions in the insulation and outer sheath layers are presented in Figs. 13(a) and (b). Stresses are concentrated in the regions where the helical wires contact the insulation and outer layers. The maximum stress in both layers was approximately 0.03 MPa. These results demonstrate that even small voltage variations in short-length cable can significantly influence the contact stresses at the interfaces.

As shown in Fig. 13(c), the average contact pressure at the insulation-armor interface increases significantly with the applied voltage. This is a direct consequence of the internal heating mechanism: the thermal expansion of the inner conductor and the thick insulation layer is constrained by the relatively cooler and stiffer outer helical armor wires. This confinement generates substantial compressive radial stress at the interface, a phenomenon that is less pronounced or absent in external heating scenarios where differential expansion is minimized. This build-up of contact pressure is the primary reason for the subsequent stiffening of the cable's bending response.

The axial stresses in the helical wires were also examined. Fig. 13(d) presents the axial stress distributions at the midpoint of each helical wire along the circumferential direction under varying voltages. Each midpoint exhibits tensile stresses, and while stress variations around the circumference are small for a given voltage, the tensile stress increases markedly as the applied voltage increases. These axial stresses significantly influence the mechanical behavior of the wires during bending, as discussed in the subsequent section.

6.2. Bending step

In this step, the electric potential was maintained while a bending angle is applied to the model. Given that the curvature–bending moment curve exhibits a two-segment behavior indicative of slip phenomena, the relative displacement between layers is of particular interest. The axial displacement of the helical wires is illustrated in Fig. 14(a).

It is observed that the axial displacement of the wires reaches its maximum positive value when the rotation angle α is near 0°, gradually decreases as α increases to 90°, and becomes increasingly negative as α approaches 180°. This behavior is further illustrated in Fig. 14(c), where the relative axial displacement between the insulation layer and the wires along the circumferential position is plotted for different applied potentials.

For all voltage cases, the wires located at the uppermost and lowermost positions exhibit the largest slip displacements, resulting in an overall cosine-shaped displacement profile. Furthermore, it is found that the higher the applied potential, the smaller the slip displacement along the wires. This is because the contact stress, enhanced by thermal expansion due to increased Joule heating, resists slip. As shown

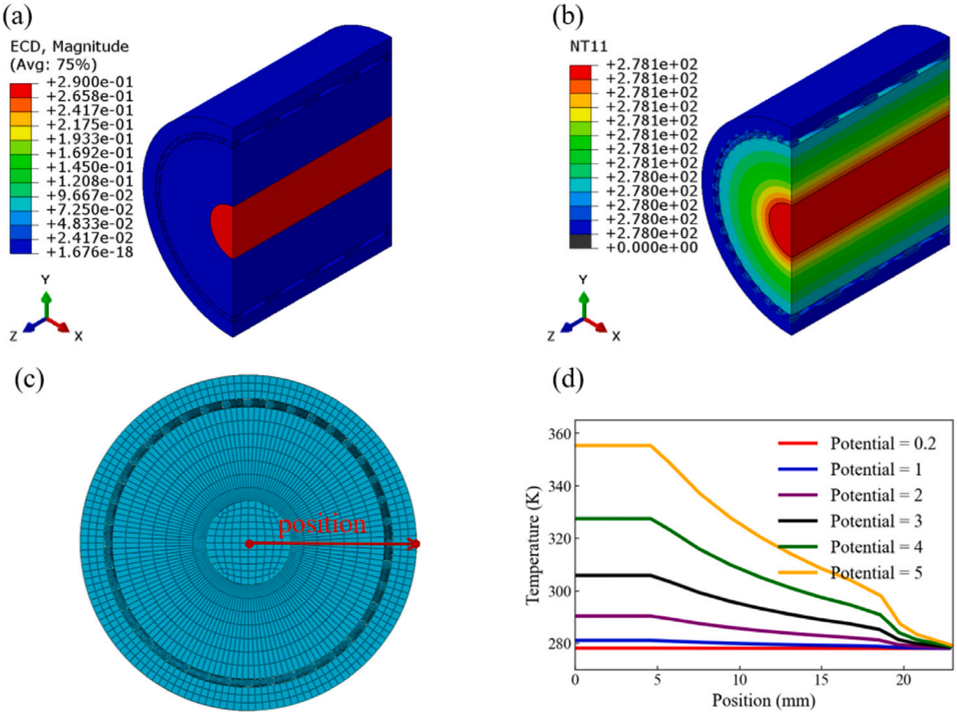

Fig. 12. Electrical current density and temperature distribution under a potential of 0.2 V: (a) electrical current density; (b) temperature distribution; (c) definition of positional direction from innermost to outermost layer; (d) temperature variation along the position for different potentials (0.2 V to 5 V).

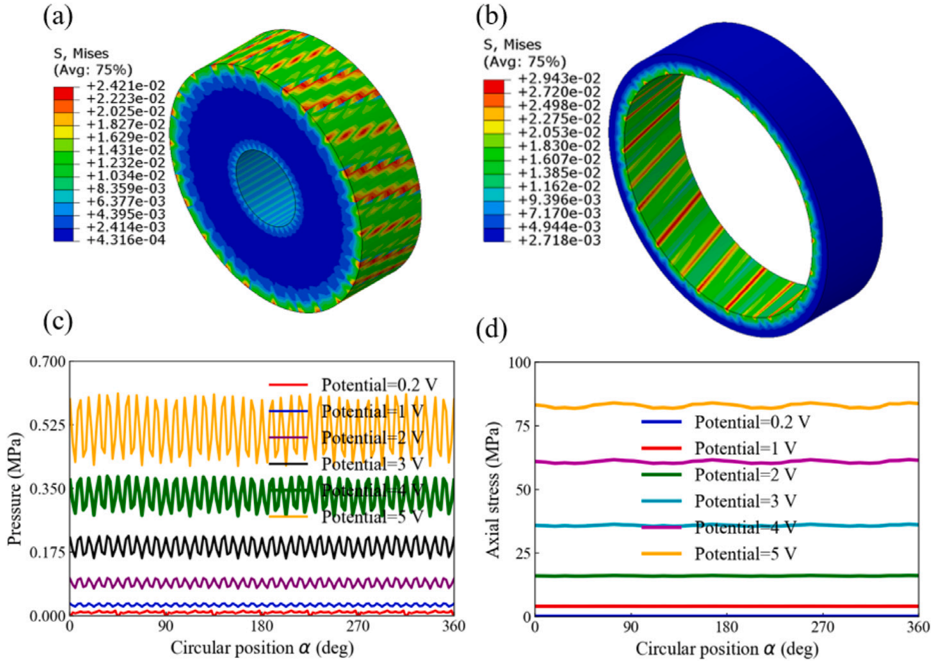

Fig. 13. Stress distributions (in MPa) in the insulation and outer layers under a potential of 0.2 V: (a) von Mises stress distribution in the insulation layer; (b) von Mises stress distribution in the outer layer; (c) variation of contact pressure along the circular position for different voltages; (d) axial stress distribution along the circular position at the end of the electric potential step.

previously in Fig. 13(c), higher potentials induce larger temperature gradients and, consequently, greater contact stresses.

As wires become more constrained under higher potentials, axial stresses begin to accumulate. The axial stress distributions along the circumferential position for various potentials are shown in Fig. 14(d). The stress profiles exhibit a sinusoidal shape. Most of the wires experience tensile stresses, while wires located between $\alpha = 220°$ and $\alpha = 330°$ are subjected to compression. The maximum tensile stress occurs around $\alpha = 90°$, while the maximum compressive stress appears around $\alpha = 270°$. These locations correspond to regions where wire slip is most difficult, as shown in Fig. 14(c).

Notably, when the applied potential is less than 4 V, all wire stresses remain below the yield limit. At 4 V, some regions around $\alpha = 90°$ start to yield, and at 5 V, yielding becomes more pronounced.

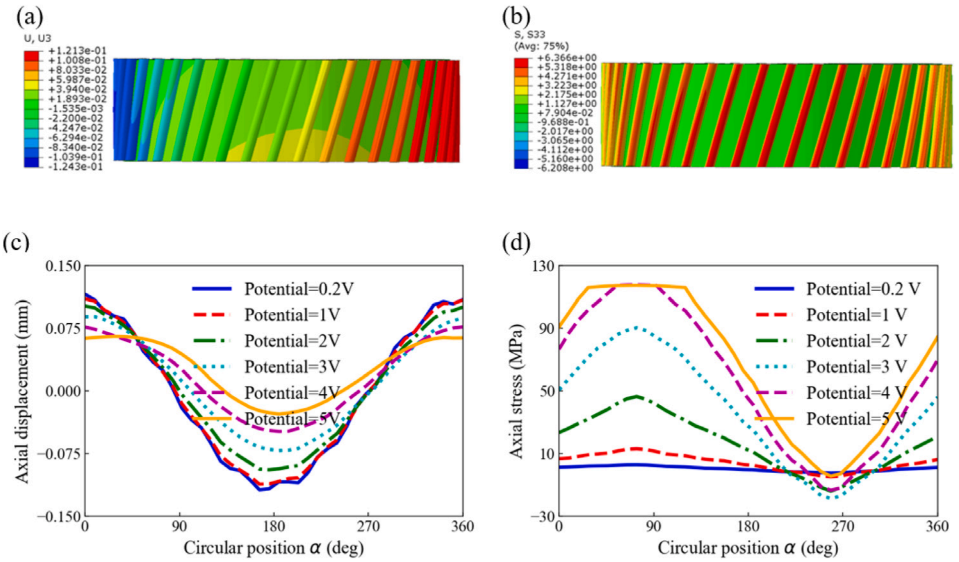

Fig. 14. Mechanical behavior of helical wires during the bending step: (a) illustration of axial displacement; (b) illustration of axial stress distribution; (c) axial displacement versus circumferential position for different applied potentials; (d) axial stress distribution versus circumferential position for different applied potentials.

The accumulation of high tensile stresses in the wires under higher potentials is attributed to pre-existing stress introduced during the electric potential step, as discussed in Fig. 13(d). Upon further bending, the upper portions of the helical wires are subjected to additional tension, exacerbating the stress state. Moreover, the proportion of wires experiencing compression decreases at higher voltages, consistent with the decreasing area below the zero-stress line observed in Fig. 13(d).

7. Parametric studies

The previous analyses have demonstrated that the friction coefficient between layers is a critical factor influencing bending performance [76,82–84]. Thus, the influence of friction coefficient is investigated in Section 7.1.

Furthermore, while it is clear that both contact forces induced by thermal expansion and variations in material properties affect bending behavior, the relative significance of each factor remains unclear due to their coupling. To decouple these effects, simulations were conducted by varying the electric potential while keeping the insulation material properties unchanged, as presented in Section 7.2.

7.1. Friction coefficient

The friction coefficient was varied from 0.1 to 0.4, in increments of 0.1, consistent with typical values for multilayer flexible structures [76,82–84]. All simulations were performed under an electric potential of 5 V, with other conditions kept constant except for the friction coefficient.

The resulting curvature–bending moment curves are shown in Fig. 15(a). The friction coefficient significantly affects the overall bending behavior, especially when changing from 0.1 to 0.2. To further explore the underlying mechanisms, the contact pressure on the outer surface of the insulation was extracted, as shown in Fig. 15(b). It is observed that variations in friction coefficient have minimal effect on the contact pressure.

Instead, notable changes occur in the axial stress within the helical wires at the end of the electric potential step, as shown in Fig. 15(c). Even small variations in contact pressure lead to noticeable differences in axial stress. Higher friction coefficients correspond to lower axial stresses within the wires. However, the difference between the maximum axial stresses for friction coefficients of 0.1 and 0.4 is only about 3.7%.

During the bending step, the helical wires start to slip for all friction coefficients. Fig. 15(d) shows that the lower the friction coefficient, the greater the slip. The most significant change occurs between coefficients of 0.1 and 0.2, where the slip difference at $\alpha = 180°$ reaches 60.3%. Increased slippage also leads to a larger reduction in wire stress, as presented in Fig. 15(e).

In the case of a friction coefficient of 0.1, the axial stresses of all wires remain below the yield limit, suggesting a lower risk of fatigue failure and improved service life in practical engineering applications [85–87].

7.2. Effect of temperature-dependent material properties

The temperature rise in the SPC induces two competing effects: thermal expansion, which increases contact stresses, and material softening of the polymers. To decouple these phenomena and quantify the sole contribution of temperature-dependent material properties, a comparative study was conducted. A second set of simulations was performed where the constitutive behavior of the XLPE insulation was held constant at its room temperature (293.15 K) properties, while the thermal expansion coefficient remained unchanged. The results were then compared against the original simulations that used the temperature-dependent material model.

The curvature–bending moment curves for both the original (temperature-dependent material) and modified (temperature-independent material) cases are compared in Fig. 16(a). It is observed that, across all cases, material property variation has a negligible effect on the overall bending behavior. The curves corresponding to the fixed and varying material properties almost completely overlap. Only at a higher electric potential of 4 V does a slight deviation between the two curves appear. This finding indicates that for current case, thermal expansion-induced contact stress variations are the dominant factor influencing the bending behavior, rather than the temperature dependence of material properties.

To further investigate this effect, the von Mises stress distributions within the insulation layer under an electric potential of 5 V were extracted for both cases, as shown in Figs. 16(b) and (c). Although differences in von Mises stress distribution are observed, the magnitudes of these stresses are extremely small. Given the relatively low stress levels in the insulation compared to the high stresses in the

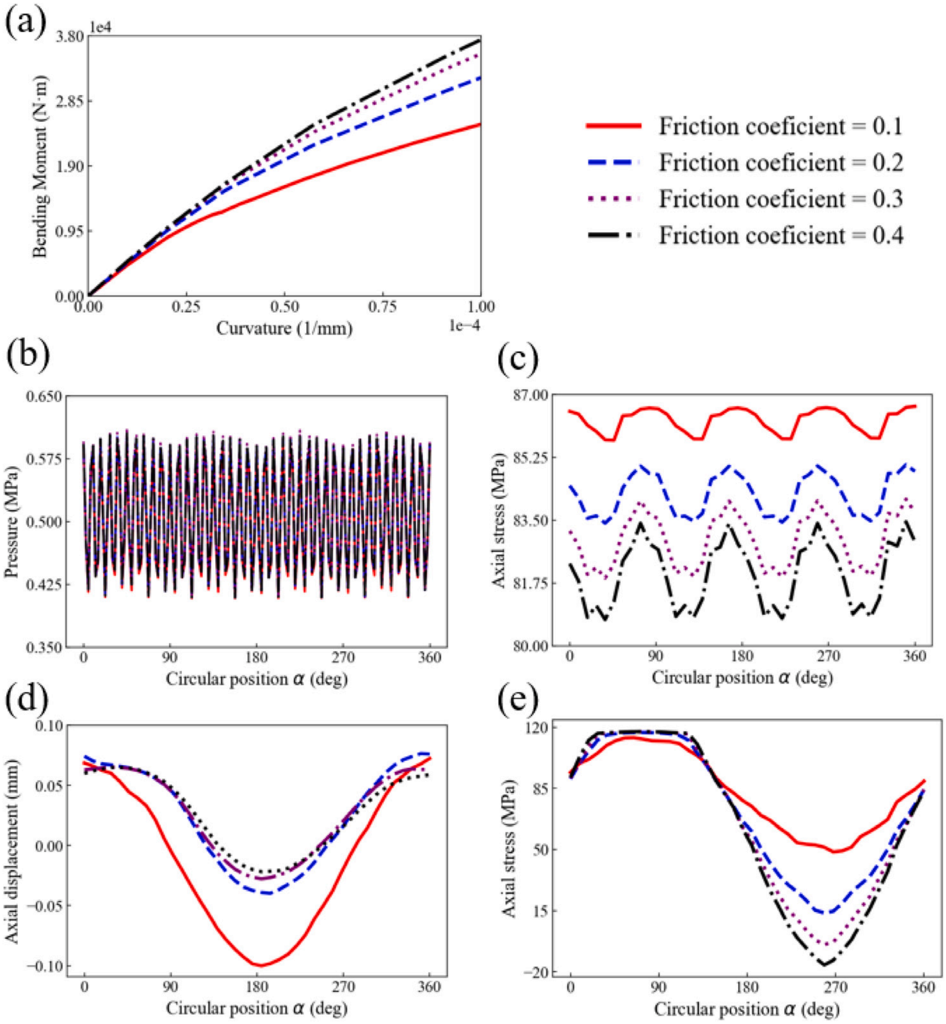

Fig. 15. Behavioral details of the SPC for friction coefficients ranging from 0.1 to 0.4 with increments of 0.1: (a) curvature–bending moment curves; (b) contact pressure on the insulation surface at the end of the electric potential step; (c) axial stress along the circumferential position for wires at the end of the electric potential step; (d) axial displacement of helical wires at the end of the bending step; (e) axial stress distribution along the circumferential position at the end of the bending step.

helical wires, these variations have little impact on the overall bending performance of the cable.

Additionally, the contact pressures on the outer surface of the insulation for the temperature-dependent and temperature-independent cases were compared, as shown in Fig. 16(d). The two pressure curves closely overlap, confirming that material property variations with temperature have minimal influence on the contact stress distribution.

This finding decisively shows that for an internally heated SPC, the stiffening effect from thermal expansion-induced contact stress overwhelmingly dominates the softening effect from the material's temperature dependency. This explains the apparent contradiction with experimental studies like those of Komperød and Magnus [44], where external heating caused a reduction in bending stiffness. In their case, the uniform temperature rise minimized internal pressure build-up, allowing the material softening effect to govern the response. Our results, however, demonstrate that under realistic operational conditions, the internal temperature gradient fundamentally alters the mechanical behavior, leading to a stiffer, not a softer, cable at higher operating currents. This highlights a critical insight for cable design and analysis: the method of heating is not just a detail but a primary factor that can reverse the expected thermo-mechanical trend.

8. Conclusions

In this study, an effective numerical model was developed to analyze the local mechanical behavior of SPCs under the combined effects of thermal and electrical fields. The model uses periodic boundary conditions in a RUC approach to enhance computational efficiency, allowing the simulation of complex cable geometries without a significant increase in computational cost. To capture the temperature-dependent material behavior of the insulation layer, a temperature-dependent constitutive model based on the Ramberg–Osgood formulation was established, with the necessary material parameters obtained through experimental tests conducted specifically on the insulation material.

The initial residual stresses within the cable's contact interfaces were simulated using the contact stresses induced by thermal expansion resulting from temperature rises. These residual stresses appear to be critical in understanding how SPCs behave under thermal and mechanical loading conditions. Four-point bending tests were conducted to calibrate the model, specifically determining the equivalent electric potential that represents the manufacturing-induced residual stresses. Following calibration, detailed mechanical analyses of SPCs under multiphysical fields (electrical, thermal, and mechanical) were

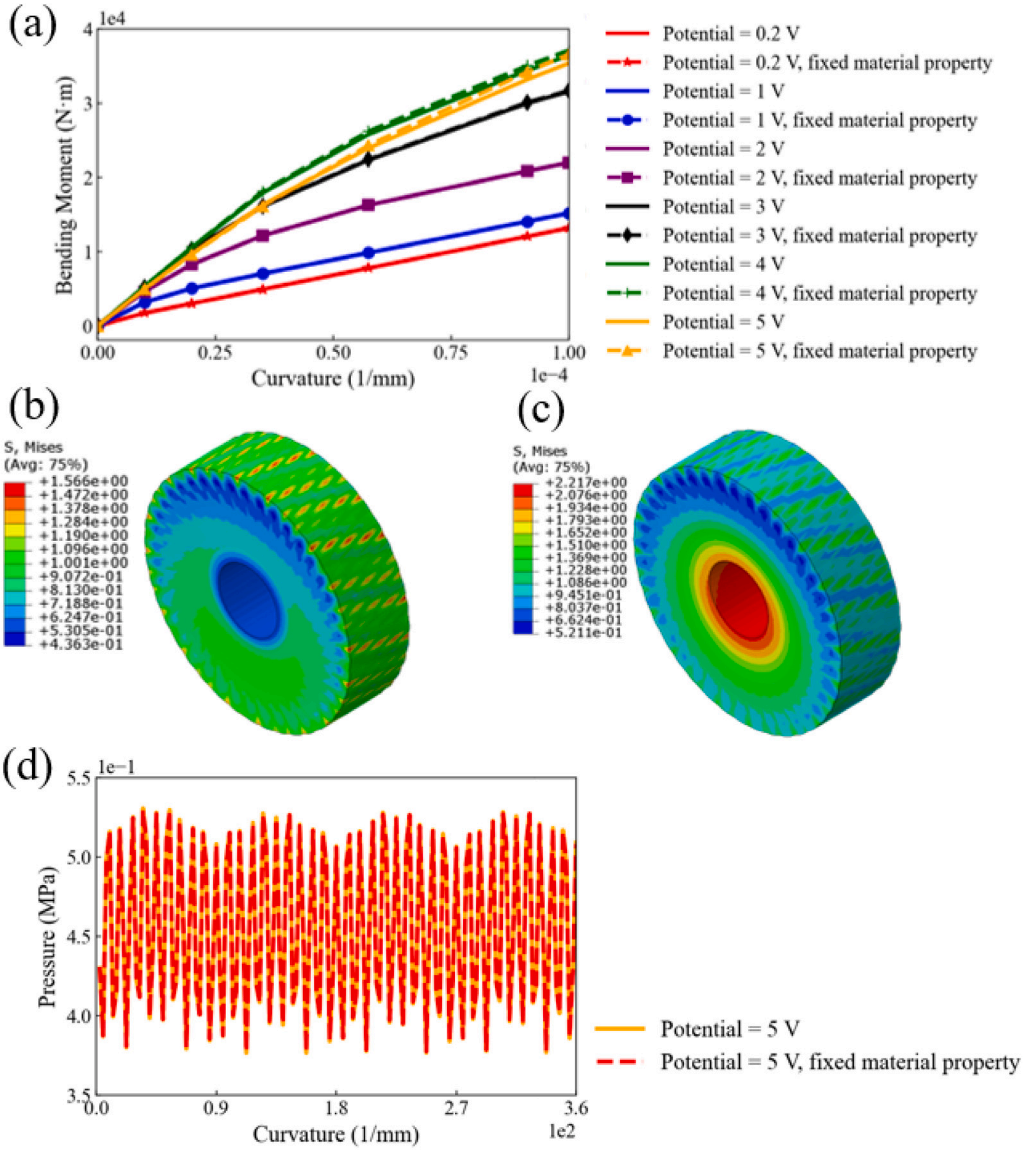

Fig. 16. Comparison of cable behavior when material properties are temperature-dependent and temperature-independent (stress and pressure are in MPa): (a) curvature–bending moment curves; (b) von Mises stress distribution in the insulation for temperature-dependent material; (c) von Mises stress distribution in the insulation for temperature-independent material; (d) contact pressure on the insulation surface for both cases.

conducted. The following key findings emerged from the study for the cable investigated in this paper:

(1) **Dominant Role of Temperature-Induced Contact Stress**: As the electric potential increased from 0 V to 5 V, the bending moment at a curvature of 1×10^{-4} mm^{-1} increased by approximately 140%. This increase can be primarily attributed to thermal expansion-induced contact stress, which significantly prolonged the stick phase in the moment–curvature response.

(2) **Minor Contribution from Material Softening**: A parametric comparison between the full temperature-dependent model and a model with material properties held constant at room temperature showed that the difference in bending moment was less than 5% for most cases. This suggests that the variation in the mechanical response was governed mainly by the change in interface contact pressure due to thermal expansion, rather than the softening of the insulation material.

(3) **Significant Impact of Friction Coefficient on Slip Behavior**: When the friction coefficient decreased from 0.4 to 0.1, the axial slip displacement of the helical wires at the most critical location (around $\alpha = 180°$) increased by over 357.9%, and the axial stress becomes less than the yield strength, indicating reduced fatigue risk.

(4) **Influence of Electric Potential on Internal Wire Stress**: For Potential = 5 V, the accumulated tensile stress in the helical wires exceeded the material yield strength locally, while for Potential < 3 V, the stress remained fully elastic. This indicates that higher electrical loading could lead to premature plastic deformation or fatigue if not accounted for.

It is important to acknowledge the limitations of the current study, which suggest avenues for future research. Firstly, the model simplifies the cable's geometry by integrating several thin functional layers into the main structural components. As discussed in Section 4, this approach, while computationally efficient, neglects localized stress concentrations and potential micro-slip at the interfaces of these thin layers, which may slightly alter the overall frictional response. Secondly, the analysis assumes quasi-static loading conditions. The rate-dependent (viscoelastic) properties of the polymeric materials were not considered, which could be significant for dynamic cables subjected to high-frequency loading. Future work should aim to develop and incorporate a rate-dependent constitutive model to capture these effects. Thirdly, while a temperature-dependent model was developed for the critical XLPE insulation, the properties of copper and MDPE were assumed to be temperature-independent and sourced from manufacturer data or previous studies. A more comprehensive experimental characterization of all components across the operational temperature range would further enhance the model's fidelity. Finally, the study employed a weak-coupling approach; a fully coupled thermo-electro-mechanical analysis, though computationally demanding, could reveal additional insights in scenarios with extreme deformations.

The modeling framework and findings presented in this study are especially relevant to practical scenarios in SPC applications. One key application is in dynamic SPCs, which are used in floating offshore wind farms and floating oil platforms. In these applications, cables are suspended and subjected to combined bending, axial tension, and thermal loading due to current-induced heating. In such configurations, the interaction between thermal expansion and contact stresses plays a critical role, potentially affecting the bending stiffness and fatigue resistance of the cable system. Additionally, thermal gradient zones, such as transitions from shallow to deep water or interfaces between seawater and air during installation, can lead to nonuniform thermal expansion and internal stress redistributions, further complicating the mechanical performance. The modeling insights from this study are also applicable to high-current steady-state operation scenarios, where sustained electrical loading induces significant temperature rises and cumulative mechanical effects, which affect long-term cable performance. These conditions highlight the importance of accurately capturing electro-thermal-mechanical coupling in the design and reliability assessment of modern SPC systems.

CRediT authorship contribution statement

Pan Fang: Writing – review & editing, Writing – original draft, Visualization, Validation, Software, Methodology, Investigation, Formal analysis, Conceptualization. **Xiao Li:** Writing – review & editing. **Xiaoli Jiang:** Writing – review & editing, Supervision. **Hans Hopman:** Writing – review & editing, Supervision. **Yong Bai:** Writing – review & editing, Supervision.

Declaration of competing interest

The authors declare the following financial interests/personal relationships which may be considered as potential competing interests: Pan Fang reports financial support was provided by China Scholarship Council [grant number 201906320047]

Acknowledgments

The first author would like to express gratitude for the support from the China Scholarship Council [grant number 201906320047] and Orient Cable (NBO) in providing the test samples.

Data availability

I have attached the link to my code in the draft.

References

[1] Taormina B, Bald J, Want A, Thouzeau G, Lejart M, Desroy N, Carlier A. A review of potential impacts of submarine power cables on the marine environment: Knowledge gaps, recommendations and future directions. Renew Sustain Energy Rev 2018;96:380–91.

[2] Yeoman M, Frizzell L, Varley R, Damodharan R. Using a multiphysics model to ensure power cables are restrained safely. In: 2015 petroleum and chemical industry conference Europe. IEEE; 2015, p. 1–9.

[3] Jeroense M. Recommendations for mechanical testing of submarine cables (and their accessories). In: Accessories for HV and EHV extruded cables: volume 2: land and submarine AC/DC applications. Springer; 2023, p. 351–424.

[4] Riley C, et al. Hv cable qualifications to iec 62067–2006 and icea s-108-720-2004. In: Jicable conf. 2011.

[5] Xu S, Wang S, Li S. Simulation analysis of 500 kv ac oil-filled submarine power cable with moisture infiltration. In: Frontier academic forum of electrical engineering. Springer; 2025, p. 145–53.

[6] Bitsi K, Chrysochos AI, Chatzipetros D, Gkitsos D. Magnetic field estimation in ac three-core armored power cables. IEEE Trans Power Deliv 2025.

[7] Hutchison ZL, Gill AB, Sigray P, He H, King JW. A modelling evaluation of electromagnetic fields emitted by buried subsea power cables and encountered by marine animals: considerations for marine renewable energy development. Renew Energy 2021;177:72–81.

[8] Scott GD, Pooley MA, Cotts BR. Numerical and analytical modeling of electromagnetic fields from offshore power distribution cables. IEEE Trans Magn 2023;59(5):1–5.

[9] Haber F. The magnetic field in the vicinity of parallel and twisted three-wire cable carrying balanced three-phased current. IEEE Trans Electromagn Compat 1974;(2):76–82.

[10] Mazzanti G, Landini M, Kandia E. A simple innovative method to calculate the magnetic field generated by twisted three-phase power cables. IEEE Trans Power Deliv 2010;25(4):2646–54.

[11] Chakraborty S, Boteler DH, Shi X, Murphy BS, Hartinger MD, Wang X, Lucas G, Baker JB. Modeling geomagnetic induction in submarine cables. Front Phys 2022;10:1022475.

[12] del Pino-López JC, Cruz-Romero P. Use of 3d-fem tools to improve loss allocation in three-core armored cables. Energies 2021;14(9):2434.

[13] Gulski E, Anders G, Jongen R, Parciak J, Siemiński J, Piesowicz E, Paszkiewicz S, Irska I. Discussion of electrical and thermal aspects of offshore wind farms' power cables reliability. Renew Sustain Energy Rev 2021;151:111580.

[14] International Electrotechnical Commission. Electric cables – calculation of the current rating – part 1-1: current rating equations (100% load factor) and calculation of losses. IEC standard 60287-1-1:2014, 2014.

[15] Zhang Y, Chen X, Zhang H, Liu J, Zhang C, Jiao J. Analysis on the temperature field and the ampacity of xlpe submarine hv cable based on electro-thermal-flow multiphysics coupling simulation. Polymers 2020;12(4):952.

[16] Dong T, Brakelmann H, Anders G. Analysis method for the design of long submarine cables. Renew Sustain Energy Rev 2023;171:113029.

[17] Mazzanti G. The combination of electro-thermal stress, load cycling and thermal transients and its effects on the life of high voltage ac cables. IEEE Trans Dielectr Electr Insul 2009;16(4):1168–79.

[18] Du Z, Li G, Yue G, Peng C, Zhan Y, Deng Y. Ampacity derating factors for submarine transmission cables in j-tubes. Electr Power Syst Res 2025;238:111118.

[19] Zhang R, Zhang S, Wang M, Peng J, Chang Z, Deng J, Wang S, Yang Y, Ma Y. Ampacity improvement of high voltage submarine cables installed in j-tubes. Electr Power Syst Res 2025;244:111562.

[20] Poradowski W, Anders G. Thermal aspects of submarine cables in bend stiffeners. Ocean Eng 2025;328:121027.

[21] Zou Z, Xu X, Wang P, Liu G. Research on enhancing heat dissipation in the air section of j-tube for submarine cables using gravity heat pipes. Appl Therm Eng 2025;270:126254.

[22] Lv Z, Rowland SM, Chen S, Zheng H, Iddrissu I. Evolution of partial discharges during early tree propagation in epoxy resin. IEEE Trans Dielectr Electr Insul 2017;24(5):2995–3003.

[23] Niemeyer L, Pietronero L, Wiesmann HJ. Fractal dimension of dielectric breakdown. Phys Rev Lett 1984;52(12):1033.

[24] Dissado L, Dodd S, Champion J, Williams P, Alison J. Propagation of electrical tree structures in solid polymeric insulation. IEEE Trans Dielectr Electr Insul 1997;4(3):259–79.

[25] Ryeskog C-A, Novljanin H. Water tree mapping in submarine high voltage cables using finite element method. 2025.

[26] Crine J-P. Electrical, chemical and mechanical processes in water treeing. IEEE Trans Dielectr Electr Insul 1998;5(5):681–94.

[27] Noguchi S, Nakamichi M, Oguni K. Proposal of finite element analysis method for dielectric breakdown based on Maxwell's equations. Comput Methods Appl Mech Engrg 2020;371:113295.

[28] Wang Q, Yang Y, Yap M, Chern WK, Chen Z. Simulating dielectric breakdown based on Maxwell's equations with inhomogeneous conductivity. In: 2022 IEEE conference on electrical insulation and dielectric phenomena. IEEE; 2022, p. 115–8.

[29] Rodríguez-Serna JM, Albarracín-Sánchez R, Carrillo I. An improved physical-stochastic model for simulating electrical tree propagation in solid polymeric dielectrics. Polymers 2020;12(8):1768.

[30] Wang Q, Deng Y, Yap M, Yang Y, Ma J, Chern WK, Li J, Chen Z. Electrical tree modelling in dielectric polymers using a phase-field regularized cohesive zone model. Mater Des 2023;235:112409.

[31] Cai Z, Wang X, Li L, Hong W. Electrical treeing: A phase-field model. Extrem Mech Lett 2019;28:87–95.

[32] Fang P, Li X, Jiang X, Hopman H, Bai Y. Development of an effective modeling method for the mechanical analysis of three-core submarine power cables under tension. Eng Struct 2024;317:118632.

[33] Ménard F, Cartraud P. A computationally efficient finite element model for the analysis of the non-linear bending behaviour of a dynamic submarine power cable. Mar Struct 2023;91:103465.

[34] Fang P, Li X, Jiang X, Hopman H, Bai Y. Methods for the local mechanical analysis of submarine power cables: A systematic literature review. Mar Struct 2025;101:103763.

[35] Chang H-C, Chen B-F. Mechanical behavior of submarine cable under coupled tension, torsion and compressive loads. Ocean Eng 2019;189:106272.

[36] Fang P, Li X, Jiang X, Hopman H, Bai Y. Development of an effective modelling method for the mechanical analysis of submarine power cables under bending. Compos Struct 2025;119198.

[37] Smith DM, Cunningham LS, Chen L. Efficient finite element modelling of helical strand cables utilising periodicity. Int J Mech Sci 2024;263:108792.

[38] Shan Z, Pham MS, Tran MT, An JS, Hwang S-K, Lee HW, Kim D-K. Efficient residual stress mitigation in additively manufactured 18ni300 maraging steel. Int J Mech Sci 2024;268:109055.

[39] Lu S, Ao N, Kan Q, Wu S, Kang G, Zhang X. Effect of residual stress in gradient-grained metals: Dislocation dynamics simulations. Int J Mech Sci 2023;256:108518.

[40] Nguyen H-G, Fang T-H. Machining mechanism and residual stress of alcucrfeni alloy. Int J Mech Sci 2024;277:109429.

[41] Sævik S. A finite element model for predicting stresses and slip in flexible pipe armouring tendons. Comput Struct 1993;46(2):219–30.

[42] Maioli P. Bending stiffness of submarine cables. In: Proceedings of the 9th international conference on insulated power cables. 2015.

[43] Tyrberg A, Tjahjanto D, Hedlund J. Bend stiffness of submarine cables—an experimental and numerical investigation. In: Proceedings of the 10th international conference on insulated power cables. 2019.

[44] Komperød M, Juvik JI, Evenset G, Slora R, Jordal L. Large-scale tests for identifying the nonlinear, temperature-sensitive, and frequency-sensitive bending stiffness of the nordlink cable. In: International conference on offshore mechanics and arctic engineering, vol. 57694, American Society of Mechanical Engineers; 2017, V05AT04A004.

[45] Thies PR, Johanning L, Dobral C. Parametric sensitivity study of submarine power cable design for marine renewable energy applications. In: International conference on offshore mechanics and arctic engineering, vol. 57663, American Society of Mechanical Engineers; 2017, V03BT02A010.

[46] Rezaiee-Pajand M, Mokhtari M, Masoodi AR. A novel cable element for nonlinear thermo-elastic analysis. Eng Struct 2018;167:431–44.

[47] Masoodi AR, Ahmadi-Kamal M. Improving composite cable performance: Nonlinear thermo-elastic analysis with temperature-dependent pretension and 3d cable elements. Case Stud Constr Mater 2023;19:e02579.

[48] Ahmadi-Kamal M, Masoodi AR. Nonlinear behavior of pretensioned sus304-nickel composite cables: Effects of concentrated stiffness and temperature sensitivity. Results Eng 2025;25:104476.

[49] Du H, Weng P, Fang C, Zhang J, Weng GJ. Mechanical-thermal coupling of carbon fiber/aluminum/silicone foams under axial loading. Int J Mech Sci 2025;110201.

[50] Akamatsu D, Matsushima K, Yamada T. Optimal design of cavity-free mechanical metamaterials exhibiting negative thermal expansion. Int J Mech Sci 2024;283:109693.

[51] Drissi-Habti M, Neginhal A, Manepalli S, Carvelli V. Fiber-optic sensors (fos) for smart high voltage composite cables—numerical simulation of multi-parameter bending effects generated by irregular seabed topography. Sensors 2022;22(20):7899.

[52] Matine A, Drissi-Habti M. On-coupling mechanical, electrical and thermal behavior of submarine power phases. Energies 2019;12(6):1009.

[53] Hamdan M, Pilgrim J, Lewin P. Analysis of thermo-mechanical stress in three core submarine power cables. IEEE Trans Dielectr Electr Insul 2020;27(4):1288–96.

[54] Yan J, Su Q, Bu Y, Yang Z, Lu Q, Yue Q. Electro–thermal–mechanical coupled analysis on two high-current composite umbilical cable cross sections. J Offshore Mech Arct Eng 2021;143(6):061802.

[55] Ech-Cheikh F, Matine A, Drissi-Habti M. Preliminary multiphysics modeling of electric high-voltage cable of offshore wind-farms. Energies 2023;16(17):6286.

[56] International Electrotechnical Commission. Electric cables – guidance for installation conditions. IEC technical report 62095:2003, 2003.

[57] Holcombe A, Hann M, Brown S, Cheng S, Rawlinson-Smith R, Nicholls-Lee R, Tosdevin T, Edwards E, Monk K. Experimental–numerical model comparison of a dynamic power cable for a floating offshore wind turbine. Ocean Eng 2025;321:120384.

[58] Chen S-y, Deng Y, Liang X, Deng X-j, Wang Z-k. Research on birdcage buckling in the armor wire of a damaged umbilical cable under compression and bending cyclic load. China Ocean Eng 2025;39(1):86–99.

[59] Fang P, Li X, Jiang X, Hopman H, Bai Y. Bending study of submarine power cables based on a repeated unit cell model. Eng Struct 2023;293:116606.

[60] ISO B, et al. lastics–determination of tensile properties. British standard, Germany, 1997.

[61] Duan X, Yuan H, Tang W, He J, Guan X. A general temperature-dependent stress–strain constitutive model for polymer-bonded composite materials. Polymers 2021;13(9):1393.

[62] Martínez-Pañeda E, Fuentes-Alonso S, Betegón C. Gradient-enhanced statistical analysis of cleavage fracture. Eur J Mech A Solids 2019;77:103785.

[63] Chen H, Ginzburg VV, Yang J, Yang Y, Liu W, Huang Y, Du L, Chen B. Thermal conductivity of polymer-based composites: Fundamentals and applications. Prog Polym Sci 2016;59:41–85.

[64] Huang C, Qian X, Yang R. Thermal conductivity of polymers and polymer nanocomposites. Mater Sci Eng: R: Rep 2018;132:1–22.

[65] Radzuan NAM, Sulong AB, Sahari J. A review of electrical conductivity models for conductive polymer composite. Int J Hydrog Energy 2017;42(14):9262–73.

[66] Lu L, Shen Y, Chen X, Qian L, Lu K. Ultrahigh strength and high electrical conductivity in copper. Science 2004;304(5669):422–6.

[67] Lukassen TV, Gunnarsson E, Krenk S, Glejbøl K, Lyckegaard A, Berggreen C. Tension-bending analysis of flexible pipe by a repeated unit cell finite element model. Mar Struct 2019;64:401–20.

[68] Buannic N, Cartraud P. Higher-order effective modeling of periodic heterogeneous beams. I. Asymptotic expansion method. Int J Solids Struct 2001;38(40–41):7139–61.

[69] Buannic N, Cartraud P. Higher-order effective modeling of periodic heterogeneous beams. II. Derivation of the proper boundary conditions for the interior asymptotic solution. Int J Solids Struct 2001;38(40–41):7163–80.

[70] Kolpakov A. Calculation of the characteristics of thin elastic rods with a periodic structure. J Appl Math Mech 1991;55(3):358–65.

[71] Cartraud P, Messager T. Computational homogenization of periodic beam-like structures. Int J Solids Struct 2006;43(3–4):686–96.

[72] Atlati S, Haddag B, Nouari M, Zenasni M. Thermomechanical modelling of the tool–workmaterial interface in machining and its implementation using the abaqus vuinter subroutine. Int J Mech Sci 2014;87:102–17.

[73] Zhu Y, Li Y, Sun J, Liu C, Xu X, Zhang K, Cheng H. Lightning damage analysis of composite bolted joint structures based on thermal-electrical-structural simulation. Compos Struct 2025;352:118720.

[74] Hariharan K, Lee M-G, Kim M-J, Han HN, Kim D, Choi S. Decoupling thermal and electrical effect in an electrically assisted uniaxial tensile test using finite element analysis. Met Mater Trans A 2015;46:3043–51.

[75] Bai Y, Liu T, Cheng P, Yuan S, Yao D, Tang G. Buckling stability of steel strip reinforced thermoplastic pipe subjected to external pressure. Compos Struct 2016;152:528–37.

[76] Dai T, Sævik S, Ye N. An anisotropic friction model in non-bonded flexible risers. Mar Struct 2018;59:423–43.

[77] Papailiou KO. Bending of helically twisted cables under variable bending stiffness due to internal friction, tensile force and cable curvature [Doctor of technical sciences thesis], Athens, Greece: ETH; 1995.

[78] Jensen C, Kvarts T, Cavaleiro P, Casals L-R, Dell'Anna G, Frelin W, Heo H, Olsen E, Lesur F, Mampaey B, Meijer S, O'rourke P, Orton H, Wilson R, Zhang R. Cigre tb 610 - offshore generation cable connections. 2015.

[79] Cornacchia F, Liu T, Bai Y, Fantuzzi N. Tensile strength of the unbonded flexible pipes. Compos Struct 2019;218:142–51.

[80] Zhao S, Zhang Y, Zhang Y, Yang J, Kitipornchai S. Graphene origami-enabled auxetic metallic metamaterials: an atomistic insight. Int J Mech Sci 2021;212:106814.

[81] Chicco D, Warrens MJ, Jurman G. The coefficient of determination r-squared is more informative than smape, mae, mape, mse and rmse in regression analysis evaluation. Peerj Comput Sci 2021;7:e623.

[82] Ji W, Ma H, Liu F, Sun W, Wang D. Dynamic analysis of cracked pipe elbows: Numerical and experimental studies. Int J Mech Sci 2024;281:109580.

[83] Dai T, Sævik S, Ye N. Friction models for evaluating dynamic stresses in non-bonded flexible risers. Mar Struct 2017;55:137–61.

[84] Zhang X, Wang S, Ma W, Su L, Yang Y. Study on the influence of bending curvature on the bending characteristics of unbonded flexible pipes. Ocean Eng 2023;281:114730.

[85] Kuznecovs A, Ringsberg JW, Yang S-H, Johnson E, Anderson A. A methodology for design and fatigue analysis of power cables for wave energy converters. Int J Fatigue 2019;122:61–71.

[86] Sobhaniasl M, Petrini F, Karimirad M, Bontempi F. Fatigue life assessment for power cables in floating offshore wind turbines. Energies 2020;13(12):3096.

[87] Thies PR, Johanning L, Smith GH. Assessing mechanical loading regimes and fatigue life of marine power cables in marine energy applications. Proc Inst Mech Eng Part O: J Risk Reliab 2012;226(1):18–32.